

Electronic and structural characteristics of a polycrystalline $\text{IrO}_2\text{:Li}/(100)$ -oriented Si pn heterojunction

ABDULLAH ALQUWAYZANI,¹ LAURENTIU BRAIC,² MOHAMED BEN HASSINE,² MOHAMED N. HEDHILI,² REDHA H. AL IBRAHIM,¹ DALAVER H. ANJUM,^{3,5} TIEN KHEE NG,¹ NASIR ALFARAJ,^{4,6} AND BOON S. OOI^{1,7}

¹Photonics Laboratory, Computer, Electrical and Mathematical Sciences and Engineering Division (CEMSE), King Abdullah University of Science and Technology (KAUST), Thuwal 23955-6900, Saudi Arabia

²Core Labs, King Abdullah University of Science and Technology (KAUST), Thuwal 23955-6900, Saudi Arabia

³Department of Physics, Khalifa University of Science and Technology, Abu Dhabi, Abu Dhabi 00000, United Arab Emirates

⁴The Edward S. Rogers Sr. Department of Electrical and Computer Engineering, University of Toronto, 10 King's College Road, Toronto, ON, M5S 3G4, Canada

⁵dalaver.anjum@ku.ac.ae

⁶nasir.alfaraj@utoronto.ca

⁷boon.ooi@kaust.edu.sa

Abstract: Achieving optimal band alignment and efficient p-type conductivity is a critical challenge for the heterogeneous integration of wide bandgap materials onto silicon (Si), a key step in revolutionizing next-generation integrated circuits (ICs). In this work, we report what we believe to be the first investigation of the heterojunction formed by pulsed laser deposition (PLD) growth of lithium-doped iridium oxide ($\text{IrO}_2\text{:Li}$) on (100)-oriented Si. The $\text{IrO}_2\text{:Li}$ films exhibit a polycrystalline structure with a preferred (200) out-of-plane orientation, as confirmed by X-ray diffraction (XRD) and transmission electron microscopy (TEM). Monochromated electron energy loss spectroscopy (EELS) measurements revealed an electronic bandgap of 2.90 eV for the $\text{IrO}_2\text{:Li}$ film, which is corroborated by photoluminescence (PL) measurements and consistent with prior work on undoped IrO_2 . Electrical characterization demonstrated p-type conductivity with a high carrier concentration, comparable to that of epitaxial IrO_2 films. The valence and conduction band offsets at the $\text{IrO}_2\text{:Li}/\text{Si}$ heterointerface were determined to be 0.76 ± 0.10 and 2.54 ± 0.10 eV, respectively, using high-resolution X-ray photoelectron spectroscopy (HRXPS), indicating a type-II (staggered) band alignment. The combination of wide bandgap, p-type conductivity, and favorable band alignment with Si makes PLD-grown $\text{IrO}_2\text{:Li}$ a promising candidate for future optoelectronic and power devices integrated with Si technology.

1. Introduction

Iridium oxides (IrO_x) have attracted considerable interest as electrode materials for oxygen evolution reaction (OER) [1], biocompatible implantable sensors and actuators [2], supercapacitors [3], pH sensors [4], electrochromic devices [5], transparent electronics [6], and spintronic applications [7]. They exhibit desirable physicochemical properties, including visible light transmission [8], adequate electrical conductivity [9], and excellent chemical stability in harsh acidic environments [10]. In particular, rutile-polymorph iridium oxide (IrO_2) is the most thermodynamically stable and extensively studied crystalline form of iridium oxide thin films. IrO_2 thin films, with varying degrees of crystallinity, have been synthesized by several methods, including reactive sputtering [6], thermal oxidation [4], pulsed laser deposition (PLD) [11], and electrochemical deposition [12]. IrO_2 thin films reported in literature predominantly exhibit

resistivity levels on the order of $10 \mu\Omega \cdot \text{cm}$, given the nature of IrO_2 as a dioxide with a rutile crystal structure with incompletely filled d shells (IrO_2 [$5d^5$]) [13]. Past investigations into the conductivity mode and majority carriers of IrO_2 have yielded varying results. The majority carrier type in IrO_2 has been shown to be affected by annealing [14], alloying [9], and deposition method [12, 15]. Density functional theory (DFT) predicts an optical bandgap value of 3.12 eV for crystalline IrO_2 [16]. Kavar et al. measured the optical bandgap values of polycrystalline thin films of IrO_2 . These films were obtained by annealing amorphous, non-stoichiometric Ir_2O_3 -phase thin films prepared by spray pyrolysis technique (SPT) on glass substrates. The measured optical bandgap values were in the range of 2.4–2.5 eV [14].

The narrow bandgap of silicon (Si), namely $E_g^{\text{Si}} = 1.12$ eV, limits its potential for deep-ultraviolet (DUV) optoelectronics [17]. Meanwhile, the performance of Si-based power electronics is steadily approaching its theoretical limits. Therefore, integrating wide-bandgap semiconductors onto Si substrates has been explored to extend the operational light spectrum in Si-based optoelectronics [18] and meet the demands for compact and energy-efficient devices. Researchers have sought to obtain polycrystalline IrO_2 thin films on Si substrates. El Khakani et al. studied the effect of substrate pretreatment on polycrystalline IrO_2 thin films grown on (100)-oriented Si by PLD [19], while Zhang et al. studied the effect of deposition temperature on the growth orientations and electrical characteristics of polycrystalline IrO_2 films grown by PLD on (100)-oriented Si substrates [5]. Moreover, Gong et al. investigated the stability of IrO_2 films grown on (100)-oriented Si under low oxygen pressure and found that the decomposition temperature of IrO_2 films decreases with decreasing oxygen pressure [11]. Recently, Cromer et al. demonstrated strong p-type conduction in crystalline IrO_2 films deposited via molecular-beam epitaxy (MBE) on beta-polymorph gallium oxide ($\beta\text{-Ga}_2\text{O}_3$) [20].

Bipolar junction devices based on wide-bandgap materials involve both p-type and n-type semiconductors. However, p-type metal oxide semiconductors are prone to crystal defects and vacancies, complicating device fabrication [21]. Doping can enhance p-type conductivity in metal oxide semiconductors. In particular, lithium (Li) doping has been demonstrated to enhance the p-type conductivity of wide-bandgap metal oxide semiconductors [22, 23]. Li-doped IrO_2 ($\text{IrO}_2\text{:Li}$) holds promise for novel optoelectronics and power electronics integrated with mature Si-based complementary metal–oxide–semiconductor (CMOS) technology. The wide bandgap, chemical stability, and potential for p-type conduction in $\text{IrO}_2\text{:Li}$ make its heterojunctions with Si promising for investigation. While the thermal stability and inertness of IrO_2 favor CMOS compatibility, [24, 25] particularly during back-end-of-line (BEOL) processes, front-end-of-line (FEOL) integration remains challenging due to higher process temperatures and potential interactions with sensitive device components [26].

In this study, we investigate for the first time the electronic and structural characteristics of $\text{IrO}_2\text{:Li}$ films grown on Si substrates by PLD and determine the energy band alignment characteristics critical for device development at an $\text{IrO}_2\text{:Li}/(100)$ -oriented Si heterojunction. Due to its wide thermodynamic range and experimental flexibility, PLD is the most widely utilized technique for growing epitaxial thin films of complex oxides [27, 28]. The polycrystalline nature and growth mode of the $\text{IrO}_2\text{:Li}$ film on Si were revealed using high-resolution X-ray diffraction (XRD), high-resolution transmission electron microscopy (HRTEM), and scanning transmission electron microscopy (STEM). Monochromated electron energy loss spectroscopy (EELS) allowed measurement of the bandgap of the $\text{IrO}_2\text{:Li}$ semiconducting film. Photoluminescence (PL) using a 213 nm excitation source was measured from the $\text{IrO}_2\text{:Li}$ film on Si to confirm the EELS measurements. These results were then compared with reported work. The resistivity, carrier concentration, and Hall mobility of the p-type $\text{IrO}_2\text{:Li}$ films on intrinsic Si were measured using the van der Pauw method. High-resolution X-ray photoelectron spectroscopy (HRXPS) was employed to examine the band offset parameters, namely the valence band offset (VBO) and conduction band offset (CBO), at the $\text{IrO}_2\text{:Li}/\text{Si}$ heterointerface. The PLD grown $\text{IrO}_2\text{:Li}$ films

first presented in this study show great potential as wide bandgap p-type semiconductors with attractive conductivity for bipolar heterojunction devices.

2. Experimental methods

Intrinsic and n-type (100)-Si wafers with single-side polish were cut into $1\text{ cm} \times 1\text{ cm}$ chips. The chips were then cleaned in ultrasonic baths of acetone, isopropyl alcohol (IPA), and deionized water, and blow-dried with nitrogen. The cleaned samples were loaded into a Neocera Pioneer 180 PLD chamber. Before film deposition, the Si chips were annealed under vacuum for one hour at a thermocouple temperature of $1000\text{ }^{\circ}\text{C}$ to remove surface oxidation. $\text{IrO}_2\text{:Li}$ films were grown in an oxygen ambient with growth pressure and temperature of 50 mTorr and $625\text{ }^{\circ}\text{C}$, respectively. A KrF laser emitting light at a wavelength of 248 nm was used. The pulsing frequency was 5 Hz with 200 mJ pulse energy and 1 J/cm^2 fluence. A ceramic PLD target comprising 1% Li and 99% IrO_2 (wt%) (99.9% purity, Plasmaterials) was used for film growth. Under the above conditions, the growth rate was determined to be around 0.066 \AA/pulse . For HRXPS measurements, films with thicknesses of 5 nm (thin) and 100 nm (thick) along with thermally treated bare Si substrate were prepared as illustrated in Fig. 1(a). The thin film sample, being thinner than the HRXPS electron extraction depth, allows probing of both the $\text{IrO}_2\text{:Li}$ and Si at the interface. In contrast, the thick film and bare Si substrate samples enabled the examination of each layer separately.

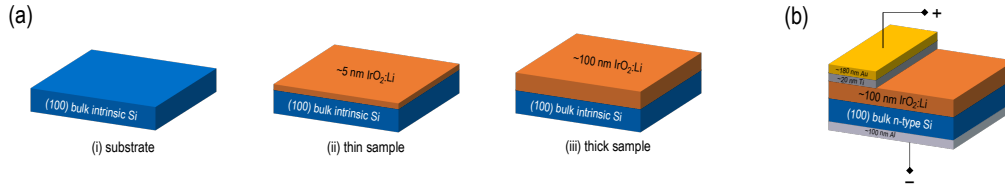


Fig. 1. (a) Schematic of the sample structures prepared for HRXPS investigation: (i) bulk Si, (ii) thin $\text{IrO}_2\text{:Li}$ film, and (iii) thick $\text{IrO}_2\text{:Li}$ film. (b) Setup for JV characterization measurements of the $\text{IrO}_2\text{:Li/Si}$ heterojunction.

Contacts with a structure of 180 nm gold (Au) on 20 nm titanium (Ti) were deposited using an Equipment Support Company (ESC) sputtering system (25 sccm Ar flow, 5 mTorr pressure, and 400 W power at room temperature with 104 and 125 sec deposition times for Ti and Au, respectively) on thick film samples. For the $\text{IrO}_2\text{:Li/n-type Si}$ heterojunction sample, the native oxide layer on the backside of the Si substrate was etched in a reactive-ion etching (RIE) chamber. The etching was performed under 1000 W of inductively coupled plasma with flow rates of 40 sccm and 5 sccm of C_4F_8 and O_2 , respectively. A 200 nm thick aluminum (Al) contact layer was sputtered (25 sccm Ar flow, 5 mTorr pressure, and 400 W power at room temperature for 715 sec) on the backside of the sample immediately after oxide removal. Current density–voltage (JV) measurements were performed on the $\text{IrO}_2\text{:Li/n-type Si}$ heterojunction sample with Ti/Au contacts to obtain the JV curves, as illustrated in Fig. 1(b). The Au/Ti contacts were also used for resistivity, Hall effect carrier concentration, and mobility measurements of $\text{IrO}_2\text{:Li}$ through the van der Pauw method.

For crystal structure analysis, out-of-plane XRD scans were obtained using a Bruker D8 Discover ($\lambda = 1.5406\text{ \AA}$) over 15° – 68° 2θ , with 1 sec/step and 0.005° step size. Secondary ion mass spectrometry (SIMS) experiments were performed using a Dynamic SIMS instrument (Hiden Analytical, Warrington, U.K.). The instrument was operated under ultrahigh vacuum conditions, typically 10^{-9} Torr. A continuous Ar^+ ion beam with an energy of 4 keV was employed to sputter the surface while the selected ions were sequentially collected using a MAXIM spectrometer equipped with a quadrupole analyzer. To avoid edge effects, ions were extracted from a small area (typically $75 \times 75\text{ }\mu\text{m}^2$) centered in the middle of the sputtered area.

(estimated to be $750 \times 750 \mu\text{m}^2$) using adequate electronic gating. Sputtering time was converted to sputtering depth assuming a constant sputtering rate. Crater depth was measured using a DektakXT stylus profiler (Bruker).

A cross-section lamella of the $\text{IrO}_2\text{:Li}$ film on Si was prepared using a Helios G4 DualBeam focused ion beam (FIB)/scanning electron microscope (SEM) system for HRTEM and STEM analysis. Thin lamellae were prepared using an in-situ lift-out technique and further thinned to electron transparency ($< 50 \text{ nm}$). The sample's structure and elemental composition were examined using a Cs-corrected microscope (Thermo Fisher Scientific) operating at an accelerating voltage and a beam current of 300 kV and 0.1 nA, respectively. Dark-field (DF) imaging was performed using STEM coupled to a HAADF detector. STEM-HAADF data were acquired with a convergence angle of 17.5 mrad. Fast Fourier transform (FFT) patterns were calculated from HRTEM images of the bulk $\text{IrO}_2\text{:Li}$ film.

The electronic bandgap of $\text{IrO}_2\text{:Li}$ was determined using STEM in conjunction with EELS. Prior to measurements, a Wien filter-based monochromator reduced the electron beam's energy spread to approximately 100 meV. The microscope was operated at 300 kV accelerating voltage. EELS experiments were performed using a Gatan Imaging Filter (GIF) Continuum 1069HR energy filter equipped with a K3 direct electron detector. The collection angle of the electron energy loss spectrometer was set to approximately 40 mrad with an energy dispersion of 15 meV. STEM-EELS spectrum-image (SI) datasets were acquired in counting mode EELS. The acquired datasets were post-processed using Gatan Microscopy Suite version 3.6 (Gatan). PL emission measurements were conducted on a thick $\text{IrO}_2\text{:Li}$ film across the visible light spectrum using a 213 nm excitation laser (Teem Photonics, PND-M00201-120). The emitted PL was collected through a 20x objective and subsequently focused into a multimode optical fiber using a 200 mm focal length lens. The PL spectrum was analyzed using an OceanOptics QE Pro spectrometer. To minimize background noise and eliminate stray light, the experiment was conducted within a black box environment, allowing for the use of extended integration times. Additionally, a 400 nm filter was employed to prevent any stray light from the laser from entering the fiber.

The resistivity, carrier concentration, and mobility of $\text{IrO}_2\text{:Li}$ films on intrinsic Si were measured using an Ecopia HMS-3000 Hall system (0.566 T magnet). The Ohmic nature of the Au/Ti contacts was verified via two-probe *IV* measurements (Supporting Information, Figure S1). *JV* characterization of $\text{IrO}_2\text{:Li}$ on n-type Si ($0.01 \Omega \cdot \text{cm}$) was performed using a grounded-stage probe station. HRXPS analysis was conducted using a Kratos Axis Supra DLD spectrometer with a monochromatic Al $K\alpha$ source (75 W) under ultra-high vacuum (10^{-9} mbar). Spectra were acquired using a $300 \mu\text{m} \times 700 \mu\text{m}$ aperture. Survey spectra were collected with a pass energy of 160 eV and a step size of 1 eV, while high-resolution spectra were collected with a pass energy of 20 eV and a step size of 0.10 eV. Samples were mounted in floating mode with charge neutralization, and binding energies were referenced to adventitious C 1s at 284.8 eV.

3. Results and discussion

Fig. 2(a) shows the out-of-plane XRD scan of the thick $\text{IrO}_2\text{:Li}$ film deposited on (100)-oriented Si. After film deposition, peaks emerge at various 2θ angles. These peaks, located at 28.0° , 34.7° , 40.1° , 54.0° , and 65.5° , are attributed to the $\text{IrO}_2\text{:Li}$ (110), (101), (200), (210), and (310) planes, respectively. The (200) plane is observed as the preferred out-of-plane orientation. XRD analysis of the deposited films reveals no peaks for metallic iridium often observed in polycrystalline iridium oxide films studied in literature [11,29]. No additional iridium oxide phases were observed. The HAADF-STEM image inset in Fig. 2(a) confirms the uniform film thickness of the thick film. The high-magnification HRTEM image in Fig. 3(a) reveals the crystalline $\text{IrO}_2\text{:Li}$ grains. The FFT analysis shown in Fig. 3(b) confirms the tetragonal nature of the $\text{IrO}_2\text{:Li}$ film with lattice parameters $a = b = 4.50 \text{ \AA}$ and $c = 3.15 \text{ \AA}$.

Based on the EELS plot in Fig. 2(b) taken from the bulk of the $\text{IrO}_2\text{:Li}$ film, the electronic

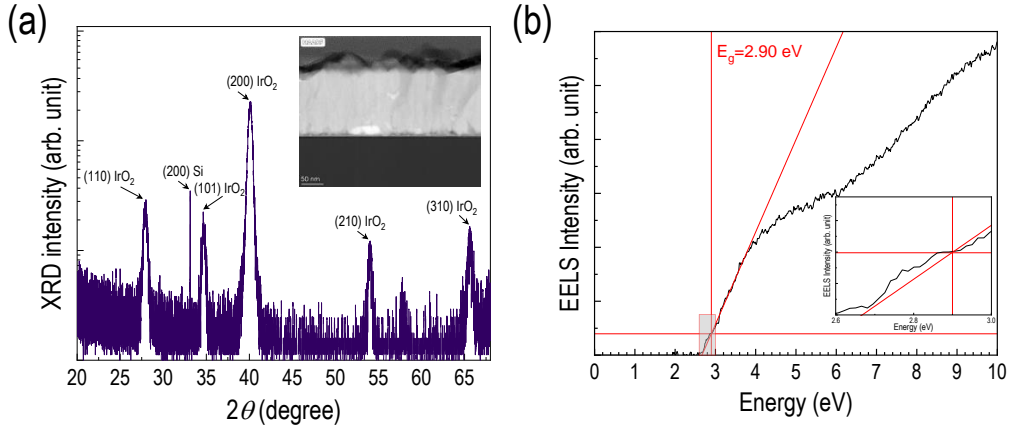


Fig. 2. (a) Out-of-plane XRD pattern of an $\text{IrO}_2\text{:Li}$ thin film grown on (100)-oriented Si. Inset: HAADF-STEM image showing the cross-section of a thick $\text{IrO}_2\text{:Li}$ film on Si. (b) EELS spectrum of the thick $\text{IrO}_2\text{:Li}$ film. Inset: Magnified view near the intersection of the baseline and the linear fit of the EELS spectrum's straight region.

bandgap is determined to be approximately 2.90 eV by extrapolating the linear region. Prior to measurement, datasets were aligned using the energy-drift routine in GMS. The zero-loss peak was then removed from the EELS spectra using the reflected tail method. The bandgap was extracted from the inelastic EELS signal using the Tauc plot method. Kramers–Kronig analysis (KKA) was also applied to the inelastic EELS signal to determine the real and imaginary parts of the dielectric function [30]. The imaginary parts were further used to find the joint density of states in the $\text{IrO}_2\text{:Li}$ film (Supporting Information, Figure S2) [31]. While the bandgap of IrO_2 has been measured through various techniques, including optical absorption [14] and ellipsometry [32], this work presents the first measurements of the bandgap of $\text{IrO}_2\text{:Li}$ in a highly controlled STEM environment.

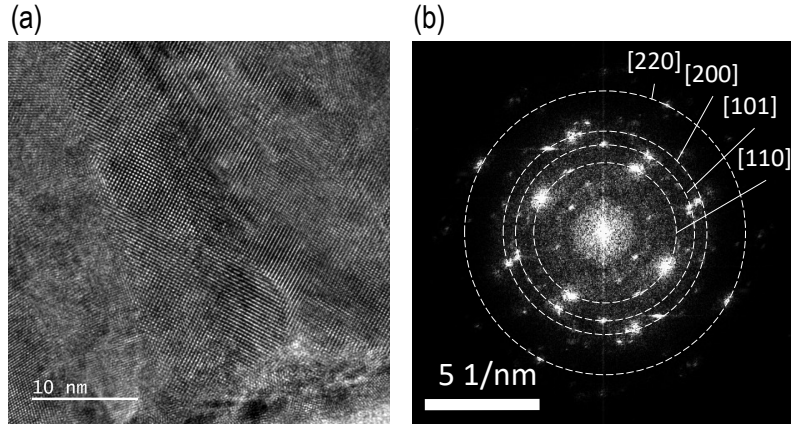


Fig. 3. (a) High-resolution HRTEM image of the bulk of the thick $\text{IrO}_2\text{:Li}$ film on Si. (b) Corresponding FFT pattern.

Fig. 4(a) reveals the bulk composition of the thick $\text{IrO}_2\text{:Li}$ film on intrinsic Si, showing a

sharp transition at the heterointerface. SIMS confirms the inclusion of Li to be uniform over the film thickness. Energy-dispersive X-ray (EDX) spectroscopy revealed elemental mapping of the cross-section (Supporting Information, Figure S3). A thin interfacial SiO_2 layer is observed, likely formed due to the high-temperature oxygen growth environment. Above the SiO_2 , a thin layer of oxygen-deficient IrO_2 :Li islands precedes the bulk IrO_2 :Li film. This behavior, which has also been observed in epitaxial IrO_2 films grown by PLD, is attributed to initial strain relaxation during grain formation [33]. EELS spectra were extracted from both the interfacial oxygen-deficient layer and the bulk IrO_2 :Li film (Supporting Information, Figure S2). Four-point probe measurements confirmed p-type conduction in the IrO_2 :Li film. These measurements yielded a resistivity of $536 \mu\Omega\cdot\text{cm}$, a carrier concentration of $5.0 \times 10^{21} \text{ cm}^{-3}$, and a mobility of $2.3 \text{ cm}^2/\text{V}\cdot\text{s}$. The semilogarithmic-scale JV curve for an IrO_2 :Li/n-type Si junction diode (Fig. 4(b)) demonstrates sustained high-voltage operation without breakdown. The rectifying behavior of the JV curve supports the formation of a pn junction.

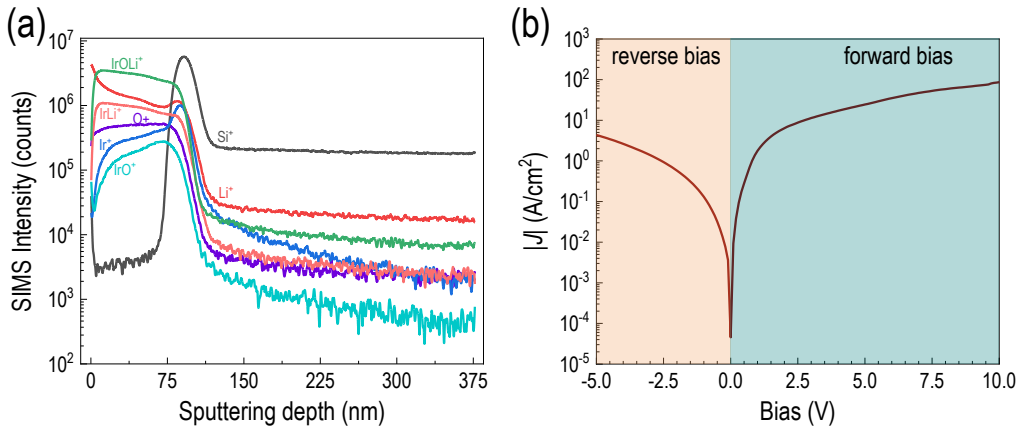


Fig. 4. (a) SIMS depth profile of the layered IrO_2 :Li/Si heterostructure. (b) Measured semilogarithmic-scale JV curve for the IrO_2 :Li/Si heterojunction.

The p-type semiconducting nature of the polycrystalline films studied in this work is a critical distinction from the crystalline films studies in earlier works. Dekkers attributed the semiconducting behavior in PLD amorphous IrO_x films to the existence of partially oxidized iridium species that are removed upon annealing the films in air [34]. A later study by Gong et al. showed that annealing in air improved both the visible light transmission and PL of IrO_2 films [11]. In contrast, the IrO_2 :Li films studied in this work exhibit both p-type conduction and a polycrystalline structure as deposited. Furthermore, the PL signal observed from the thick IrO_2 :Li film shown in Fig. 5 overlaps with the previously reported PL spectrum by Gong et al. for IrO_2 . The measured PL signal agrees with the bandgap value extracted from the EELS analysis. Although Li doping of IrO_2 is predicted to alter its electronic structure [35], the obtained hole concentration and mobility values for IrO_2 :Li are comparable to those reported for crystalline IrO_2 films. Cromer et al. measured the electrical properties of MBE grown crystalline IrO_2 with a (100) out-of-plane orientation revealing p-type conduction with a hole concentration and mobility values of $1.39 \times 10^{22} \text{ cm}^{-3}$ and $4.85 \text{ cm}^2/\text{V}\cdot\text{s}$, respectively [20]. The comparable carrier concentration and mobility to MBE-grown crystalline IrO_2 films suggest that this work offers a route to obtain p-type semiconductors based on IrO_2 without stringent epitaxial constraints.

A study conducted by Nair et al. on the anisotropy of the electric conductivity of IrO_2 grown on (110), (101), and (001) oriented TiO_2 substrates by MBE provides insight on the origin of p-type conduction in crystalline IrO_2 [36]. They found that electron and hole concentrations, as

well as mobilities, vary significantly with growth direction, leading to a switch in the majority carrier type. Since XRD analysis revealed (100) as the dominant out-of-plane orientation of our IrO₂:Li films, we believe that both film orientation and Li doping contribute to the observed p-type conduction. The anisotropy observed by Nair et al. explains why the p-type conduction observed by Cromer et al. in crystalline IrO₂, with (100) out-of-plane direction, is similar to the p-type conduction observed in the polycrystalline IrO₂:Li films studied here. However, previous works on crystalline IrO₂ did not report bandgap values, hindering direct comparison.

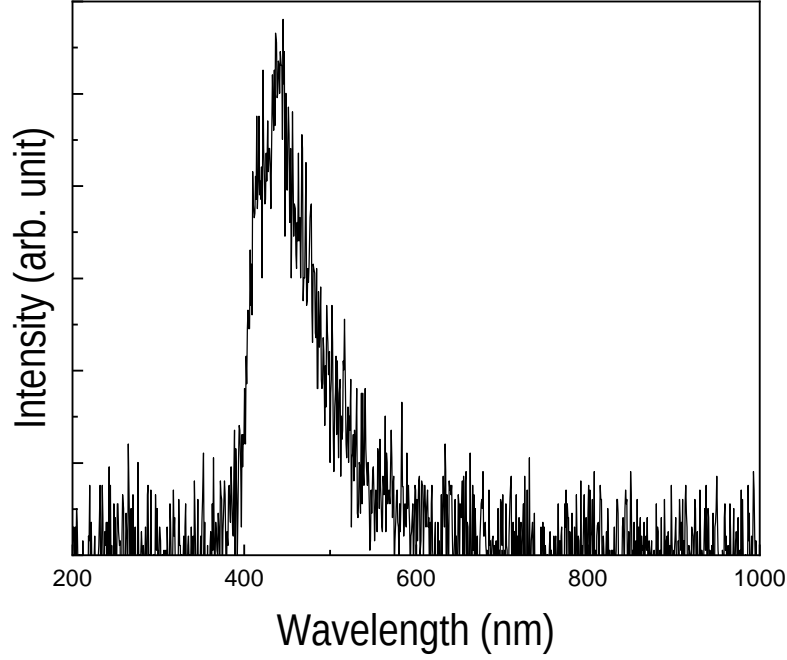


Fig. 5. PL spectrum of the thick IrO₂:Li film on Si.

To estimate the VBO and CBO at the IrO₂:Li/Si heterointerface, we need to determine several energy differences using HRXPS. First, we need the energy difference between the Si 2p_{3/2} and Ir 4f_{7/2} core levels at the interface. Second, we need the energy differences between the Si 2p_{3/2} and Ir 4f_{7/2} core levels and their respective valence band maxima (VBM) for both the Si substrate and the IrO₂:Li thick film. These values are then used in the Kraut equations [37]:

$$\begin{aligned} \Delta E_V = & (E_{\text{Ir } 4f_{7/2}}^{\text{thick IrO}_2:\text{Li}} - E_{\text{VBM}}^{\text{thick IrO}_2:\text{Li}}) \\ & - (E_{\text{Si } 2p_{3/2}}^{\text{Si}} - E_{\text{VBM}}^{\text{Si}}) \\ & + (E_{\text{Si } 2p_{3/2}}^{\text{thin IrO}_2:\text{Li}/\text{Si}} - E_{\text{Ir } 4f_{7/2}}^{\text{thin IrO}_2:\text{Li}/\text{Si}}), \end{aligned} \quad (1)$$

$$\Delta E_C = (E_g^{\text{IrO}_2:\text{Li}} - E_g^{\text{Si}}) + \Delta E_V. \quad (2)$$

Fig. 6(a) shows the Ir 4f core-level and valence band spectra of thick IrO₂:Li film sample. The binding energy of Ir 4f_{7/2} is equal to 61.90 eV and VBM is equal to 0.00 eV. The separation between the core-level energy of Ir 4f_{7/2} and valence band maximum $\Delta E_{\text{Ir } 4f_{7/2} - \text{VBM}}^{\text{IrO}_2:\text{Li}} = (E_{\text{Ir } 4f_{7/2}}^{\text{IrO}_2:\text{Li}} - E_{\text{VBM}}^{\text{IrO}_2:\text{Li}})$

for the $\text{IrO}_2\text{:Li}$ sample is determined to be 61.90 eV. Fig. 6(b) shows the Si $2p$ core-level and valence band spectra of the bulk Si sample. The binding energy of Si $2p_{3/2}$ is 99.24 eV, and the VBM is at 0.39 eV. Therefore, the separation between the Si $2p_{3/2}$ core-level energy and the VBM, $\Delta E_{\text{Si } 2p_{3/2} - \text{VBM}}^{\text{Si}} = (E_{\text{Si } 2p_{3/2}}^{\text{Si}} - E_{\text{VBM}}^{\text{Si}})$, is 98.85 eV. Fig. 6(c) shows the Ir $4f$ and Si $2p$ core level spectra of the thin $\text{IrO}_2\text{:Li}$ film grown on Si sample. The binding energies of Ir $4f_{7/2}$ and Si $2p_{3/2}$ are 99.36 eV and 61.65 eV, respectively. The energy difference between Si $2p_{3/2}$ and Ir $4f_{7/2}$ core-levels $\Delta E_{\text{Si } 2p_{3/2} - \text{Ir } 4f_{7/2}}^{\text{thin IrO}_2\text{:Li/Si}} = (E_{\text{Si } 2p_{3/2}}^{\text{thin IrO}_2\text{:Li/Si}} - E_{\text{Ir } 4f_{7/2}}^{\text{thin IrO}_2\text{:Li/Si}})$ is observed to be 37.71 eV. Substituting these values into Eq. (1) yields a VBO of 0.76 eV. The bandgap values of $\text{IrO}_2\text{:Li}$ film and Si are 2.90 and 1.12 eV, respectively. Subsequently, substituting the VBO (ΔE_V) from HRXPS analysis and the bandgap (E_g) values of $\text{IrO}_2\text{:Li}$ and Si into Eq. (2) allows us to determine the CBO at the $\text{IrO}_2\text{:Li/Si}$ heterojunction. Hence, the measured CBO (ΔE_C) is 2.54 eV. The determined offset parameters from this study are represented as a schematic of band alignment diagram in Fig. 6(d), which shows that this band alignment pertains to type-II (staggered) heterojunction. Therefore, the PLD-grown $\text{IrO}_2\text{:Li}$ investigated in this study presents a promising new p-type semiconductor for bipolar optoelectronic devices.

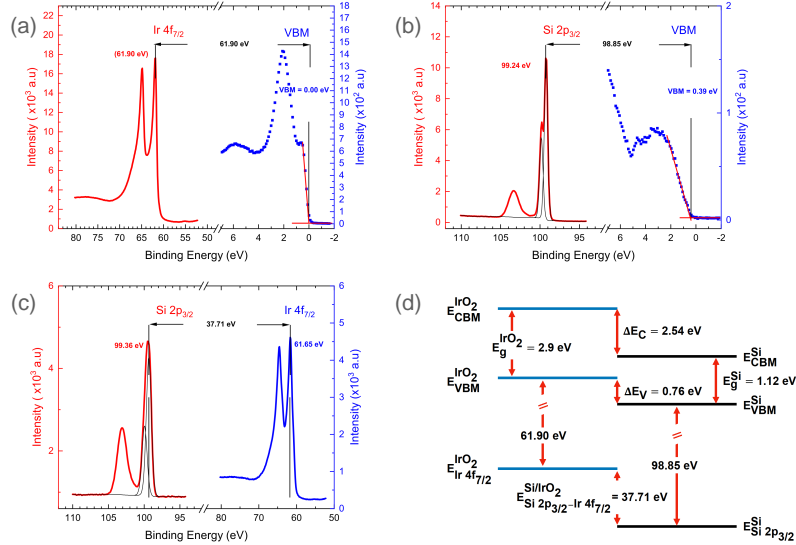


Fig. 6. HRXPS analysis: (a) Ir $4f$ and valence band spectra for $\text{IrO}_2\text{:Li}$ film; (b) Si $2p$ and valence band spectra for Si; (c) Ir $4f$ and Si $2p$ core-level spectra for the $\text{IrO}_2\text{:Li/Si}$ heterojunction; (d) Schematic band alignment diagram of the $\text{IrO}_2\text{:Li/Si}$ heterojunction.

4. Concluding remarks

This work presents the first investigation of the heterojunction formed by PLD growth of $\text{IrO}_2\text{:Li}$ on (100)-oriented intrinsic and n-type Si. The grown $\text{IrO}_2\text{:Li}$ films were polycrystalline, p-type, and exhibited a high carrier concentration. SIMS experiments revealed a sharp layer transition at the heterointerface. EELS determined an electronic bandgap of 2.90 eV for the $\text{IrO}_2\text{:Li}$ film. PL measurements confirm this bandgap and also agree with work reported in the literature. JV characterization of the $\text{IrO}_2\text{:Li/n-type Si}$ heterojunction demonstrated rectifying behavior with no breakdown observed up to 10 V. HRXPS investigation of the heterointerface revealed a staggered heterojunction. The high p-type carrier concentration of the $\text{IrO}_2\text{:Li}$ films makes them promising for thin-film power devices and visible-light optoelectronics based on staggered junctions. The

discovered optical and electrical properties of IrO₂:Li films detailed in this paper pave the way for the heterogeneous integration of IrO₂:Li in wide-bandgap bipolar devices on Si.

Funding. King Abdullah University of Science and Technology (BAS/1/1614-01-01, GEN/1/6031-01-02, URF/1/5079-01-01).

Acknowledgment. N. A. acknowledges the support of the Ibn Rushd Postdoctoral Fellowship Program, administered by KAUST, and funding provided under GEN/1/6031-01-02 from KAUST's Office of the Provost. T. K. N. and B. S. O. gratefully acknowledge the KAUST Transition Award in Semiconductors, FCC/1/5939.

Disclosures. The authors declare no conflicts of interest.

Data Availability Statement. Data underlying the results presented in this paper are not publicly available at this time but may be obtained from the authors upon reasonable request.

Supplemental document. See Supplement 1 for supporting content.

References

1. F. Liao, K. Yin, Y. Ji, *et al.*, "Iridium oxide nanoribbons with metastable monoclinic phase for highly efficient electrocatalytic oxygen evolution," *Nat. Commun.* **14**, 1248 (2023).
2. G. Taylor, R. Paladines, A. Marti, *et al.*, "Electrochemical enhancement of reactively sputtered rhodium, ruthenium, and iridium oxide thin films for neural modulation, sensing, and recording applications," *Electrochim. Acta* **394**, 139118 (2021).
3. Y.-Q. Shao, Z.-Y. Yi, C. He, *et al.*, "Effects of annealing temperature on the structure and capacitive performance of nanoscale Ti/IrO₂-ZrO₂ electrodes," *J. Am. Ceram. Soc.* **98**, 1485 (2015).
4. F. Huang, Y. Qin, Q. Wang, *et al.*, "Insight into factors influencing thermal oxidation of iridium oxide electrode: Thermostatic post-treatment temperature," *J. Electrochem. Soc.* **169**, 037530 (2022).
5. L. M. Zhang, Y. S. Gong, C. B. Wang, *et al.*, "Substrate temperature dependent morphology and resistivity of pulsed laser deposited iridium oxide thin films," *Thin Solid Films* **496**, 371 (2006).
6. M. Zubkins, R. Kalendarev, J. Gabrusenoks, *et al.*, "Structural, electrical and optical properties of zinc-iridium oxide thin films deposited by DC reactive magnetron sputtering," *Phys. Status Solidi C* **11**, 1493 (2014).
7. P.-Y. Chien, C.-Y. Wu, R.-T. Wang, *et al.*, "Quantum-interference origin and magnitude of $1/f$ noise in dirac nodal line IrO₂ nanowires at low temperatures," *Appl. Phys. Lett.* **122** (2023).
8. S. Ito, Y. Abe, M. Kawamura, *et al.*, "Electrochromic properties of iridium oxide thin films prepared by reactive sputtering in O₂ or H₂O atmosphere," *Phys. Status Solidi B* **33** (2015).
9. M. Zubkins, J. Timoshenko, J. Gabrusenoks, *et al.*, "Amorphous p-type conducting Zn-xIr oxide ($x > 0.13$) thin films deposited by reactive magnetron cosputtering," *Phys. Status Solidi (b)* **259**, 2100374 (2022).
10. Q. Dang, H. Lin, Z. Fan, *et al.*, "Iridium metallene oxide for acidic oxygen evolution catalysis," *Nat. Commun.* **12**, 6007 (2021).
11. Y. Gong, C. Wang, Q. Shen, *et al.*, "Thermal stability of pulsed laser deposited iridium oxide thin films at low oxygen atmosphere," *Appl. Surf. Sci.* **285**, 324 (2013).
12. L. Ilyukhina, S. Sunde, and R. G. Haverkamp, "Electronic structure and growth of electrochemically formed iridium oxide films," *J. Electrochem. Soc.* **164**, F1662 (2017).
13. J. Riga, C. Tenret-Noel, J.-J. Pireaux, *et al.*, "Electronic structure of rutile oxides TiO₂, RuO₂ and IrO₂ studied by X-Ray photoelectron spectroscopy," *Phys. Scr.* **16**, 351 (1977).
14. R. K. Kwar, P. S. Chigare, and P. S. Patil, "Substrate temperature dependent structural, optical and electrical properties of spray deposited iridium oxide thin films," *Appl. Surf. Sci.* **206**, 90 (2003).
15. A. Avila-García, A. Chaudhary, and H. Rojas-Chávez, "Iridium oxide films as propane sensors," *Thin Solid Films* **724**, 138617 (2021).
16. S. H. Brewer, D. Wicaksana, J.-P. Maria, *et al.*, "Investigation of the electrical and optical properties of iridium oxide by reflectance FTIR spectroscopy and density functional theory calculations," *Chem. Phys.* **313**, 25 (2005).
17. M. Kneissl, T.-Y. Seong, J. Han, *et al.*, "The emergence and prospects of deep-ultraviolet light-emitting diode technologies," *Nat. Photonics* **13**, 233–244 (2019).
18. N. Alfaraj, K.-H. Li, C. H. Kang, *et al.*, "Silicon-integrated monocrystalline oxide-nitride heterostructures for deep-ultraviolet optoelectronics," *Opt. Mater. Express* **11**, 4130–4144 (2021).
19. M. A. El Khakani, M. Chaker, and E. Gat, "Pulsed laser deposition of highly conductive iridium oxide thin films," *Appl. Phys. Lett.* **69**, 2027 (1996).
20. B. Cromer, D. Saraswat, N. Pieczulewski, *et al.*, "Over 6 MV/cm operation in β -Ga₂O₃ schottky barrier diodes with IrO₂ and RuO₂ anodes deposited by molecular beam epitaxy," *J. Vac. Sci. Technol. A* **42** (2024).
21. Z. Zhang, B. Liu, F. Quinteros, *et al.*, "Understanding the role of oxygen and hydrogen defects in modulating the optoelectronic properties of p-type metal oxide semiconductors," *Chem. Mater.* **33**, 7829 (2021).

22. M. M. Walid, R. Singh, N. E.-C. Abdelkader, *et al.*, "Insights into spray-coated p-type Li-doped ZnO thin films: An examination of structural, chemical, optical, and electrical characteristics," *MRS Adv.* pp. 1–7 (2024).
23. J. Y. Zhang, W. W. Li, R. L. Z. Hoye, *et al.*, "Electronic and transport properties of Li-doped NiO epitaxial thin films," *J. Mater. Chem. C* **6**, 2275–2282 (2018).
24. M. A. Pawlak, T. Schram, K. Maex, *et al.*, "Investigation of iridium as a gate electrode for deep sub-micron CMOS technology," *Microelectron. Eng.* **70**, 373 (2003).
25. S. R. Summerfelt, L. H. Hall, K. R. Udayakumar, and T. S. Moise IV, "Ferroelectric capacitor stack etch cleaning methods," (2007). US Patent 7,220,600.
26. N. Alfaraj, C. C.-C. Lin, S. Nasif, *et al.*, "Facile integration of electro-optic SiO₂/ITO heterointerfaces in MIS structures for CMOS-compatible plasmonic waveguide modulation," *Light Adv. Manuf.* **4**, 420–436 (2023).
27. N. A. Shepelin, Z. P. Tehrani, N. Ohannessian, *et al.*, "A practical guide to pulsed laser deposition," *Chem. Soc. Rev.* **52**, 2294–2321 (2023).
28. N. Alfaraj, K.-H. Li, M. Alaweini, *et al.*, "Heteroepitaxial β -Ga₂O₃ on conductive ceramic templates: Toward ultrahigh gain deep-ultraviolet photodetection," *Adv. Mater. Technol.* **6**, 2100142 (2021).
29. P. Marsh, M.-H. Huang, X. Xia, *et al.*, "Polarization conforms performance variability in amorphous electrodeposited iridium oxide pH sensors: A thorough surface chemistry investigation," *Sensors* **24**, 962 (2024).
30. R. F. Egerton, "Electron energy-loss spectroscopy in the TEM," *Rep. Prog. Phys.* **72**, 016502 (2008).
31. V. J. Keast, "Ab initio calculations of plasmons and interband transitions in the low-loss electron energy-loss spectrum," *J. Electron Spectrosc. Relat. Phenom.* **143**, 97–104 (2005).
32. R. Sachse, M. Pflüger, J.-J. Velasco-Vélez, *et al.*, "Assessing optical and electrical properties of highly active IrO_x catalysts for the electrochemical oxygen evolution reaction via spectroscopic ellipsometry," *ACS Catal.* **10**, 14210–14223 (2020).
33. X. Hou, R. Takahashi, T. Yamamoto, *et al.*, "Microstructure analysis of IrO₂ thin films," *J. Cryst. Growth* **462**, 24–28 (2017).
34. J. M. Dekkers, "Transparent conducting oxides on polymeric substrates by pulsed laser deposition," Ph.D. thesis, University of Twente (2007).
35. Y. Shan, Q. Gao, Y. Zhu, *et al.*, "Indirect orbital hybridization induced by nonbonding interaction at Li-intercalated IrO₂ monolayers for oxygen evolution reaction," *Phys. Status Solidi - Rapid Res. Lett.* **17**, 2300093 (2023).
36. S. Nair, Z. Yang, K. Storr, *et al.*, "High-mobility carriers in epitaxial IrO₂ films grown using hybrid molecular beam epitaxy," (2024).
37. E. A. Kraut, R. W. Grant, J. R. Waldrop, *et al.*, "Precise determination of the valence-band edge in X-Ray photoemission spectra: Application to measurement of semiconductor interface potentials," *Phys. Rev. Lett.* **44**, 1620 (1980).